Paper No.
2291

NACE INTERNATIONAL CORROSION 2013 CONFERENCE & EXPO

Iron Carbide and its Influence on the Formation of Protective Iron Carbonate in CO_2 Corrosion of Mild Steel

F. Farelas, B. Brown and S. Nesic
Institute for Corrosion and Multiphase Technology,
Department of Chemical & Biomolecular Engineering,
Ohio University, Athens, OH 45701, USA

ABSTRACT

The present research studied the role porous iron carbide layers (Fe_3C) on the formation of protective iron carbonate ($FeCO_3$). Two mild steels with similar carbon content and different microstructure were chosen. API[1] 5L X65 and UNS[2] G10180 steels with tempered martensite and ferrite - pearlite microstructures, respectively, were exposed to a 3 wt.% NaCl-CO_2 saturated solution at pH 6 and 80°C in laminar flow. The corrosion behavior was monitored by linear polarization resistance (LPR) during long term experiments. Electrochemical measurements were supported by surface analytical techniques (Scanning electron microscopy (SEM) and energy-dispersive X-ray spectroscopy (EDS)). A porous Fe_3C layer was observed for both steels during the first days of exposure, although morphology was different due to the steel microstructure. With time, the iron carbide layers observed for both steels acted as a diffusion barrier for ferrous and carbonate ions, resulting in a high surface pH, so that when the solubility limit of $FeCO_3$ was exceeded, a protective $FeCO_3$ scale formed within the porous layer regardless of the steel microstructure.

Key words: CO_2 corrosion, carbide, iron carbonate, steel microstructure

[1] American Petroleum Institute (API), 1220 L St. NW, Washington, DC 20005.
[2] Unified Numbering System for Metals and Alloys (UNS). UNS numbers are listed in Metals & Alloys in the Unified Numbering System, 10th ed. (Warrendale, PA: SAE International and West Conshohocken, PA: ASTM International, 2004).

INTRODUCTION

The effect of corrosion products on the performance of mild steel when exposed to CO_2 environments is crucial for the protection of pipelines from internal corrosion. The presence of different microstructural phases in mild steel may lead to separation of anodic and cathodic sites that affect directly the rate of metal dissolution.[1, 2] As a result of corrosion, different corrosion products can form on the metal surface that might protect it from further dissolution. One of the most common corrosion products found in CO_2 corrosion of mild and low-alloy steels is a mixture of iron carbide (Fe_3C) and iron carbonate ($FeCO_3$).[3] Fe_3C is the part of the steel microstructure and its quantity increases with the carbon content of the steel.[4] Fe_3C is more difficult to dissolve than the ferrite phase (α-Fe) and it is often found left on the metal surface as a consequence of the corrosion process. It is believed that, since Fe_3C is an electronic conductor, its presence enhances the corrosion rate by causing a galvanic effect and acting as a cathodic site for the hydrogen evolution reaction (HER).[5, 6] However, the presence of Fe_3C is not always detrimental. Under some environmental conditions (high pH, temperature, pCO_2, ferrous ion concentration and low flow rate), it has been observed that the Fe_3C layer may help to form and anchor a $FeCO_3$ layer, which protects the mild steel surface from corrosion.[7, 8]

The formation of protective $FeCO_3$ depends on temperature, pH and $FeCO_3$ saturation value, among other factors. At low bulk $FeCO_3$ saturation values, pH between 5.5 and 6 and 60°C, thick non-protective porous Fe_3C layers have been observed on ferritic-pearlitic steels, both in laboratory tests and in the field.[7] Dugstad[7] reported that the porous Fe_3C acted as a substrate for $FeCO_3$ precipitation when the degree of supersaturation is increased (10 - 100 times). High supersaturation values lead to massive $FeCO_3$ precipitation inside the Fe_3C layer and its protectiveness depended on temperature. At 80°C $FeCO_3$ formed inside the Fe_3C layer close to the metal, offering good corrosion protection. On the other hand, at 60°C $FeCO_3$ started to grow at the outer surface and inwards, which was poorly protective.

The importance of Fe_3C in the formation of $FeCO_3$ has been acknowledged recently and several attempts to form Fe_3C and $FeCO_3$ layers in glass cell experiments have been made.[9, 10] Berntsen *et al*.,[9] performed experiments in order to understand the effect $FeCO_3$ supersaturation and Fe_3C on the formation of protective $FeCO_3$ in a system with 50wt.% glycol at 20°C. API 5L X65 samples were pre-corroded with the aim of leaving an exposed Fe_3C layer on top of the steel surface, followed by an increase in the $FeCO_3$ supersaturation level. Authors reported that it was not possible to form a protective $FeCO_3$ under the proposed experimental conditions, regardless of the high supersaturation levels. The authors attributed that behaviour to the insufficient amount of Fe_3C formed during the pre-corrosion process, since the presence of Fe_3C in believed to be a key parameter for growth of $FeCO_3$, besides the supersaturation value.

The present paper focuses on understanding the role Fe_3C on the formation of protective $FeCO_3$. Two different carbon steels with tempered martensite and ferrite - pearlite microstructures were selected for this study. Steel samples were exposed a 3 wt.% NaCl solution saturated with CO_2 at pH 6 and 80°C. In order to eliminate the effect of the centrifugal forces found with rotating cylinder electrodes, a recirculating flow loop (170 L) and a thin channel flow cell were used. Linear polarization resistance (LPR) was used to estimate the change in corrosion rate with time during long term experiments. Surface characterization techniques such as scanning electron microscopy (SEM) and energy dispersive X-ray spectroscopy (EDS) were used to characterize the morphology and chemical composition of the corrosion products formed on steel samples.

EXPERIMENTAL PROCEDURE

System Preparation

In order to simulate turbulent flow condition, the experiments were conducted in a flow loop called Thin Channel Flow Cell (TCFC). The most important part is the test section (Figure 1) in the form of a flow

channel with a very high aspect ratio (3 mm x 100 mm) used to create well controlled fully developed turbulent channel flow. Corrosion samples and electrodes are inserted flush mounted at the bottom of the channel.

The flow loop was first filled with a 3 wt.% NaCl aqueous solution that was continuously purged with CO_2 during the whole test to remove oxygen and maintain a constant concentration of dissolved CO_2. During the purging process, the solution temperature was increased to 80ºC. After 12 h allowed for further equilibration, the pH of the test solution was adjusted from the equilibrium pH (pH = 4.3 ± 0.10) to the desired pH by adding a deoxygenated sodium hydroxide solution (NaOH). Once the pH was adjusted and stable, an electrochemical probe and three cylindrical steel samples, used for surface and chemical analysis, were flush mounted at the bottom of a dry test section filled with CO_2, and only then the flow was diverted into the test section. Experimental conditions are summarized in Table 1.

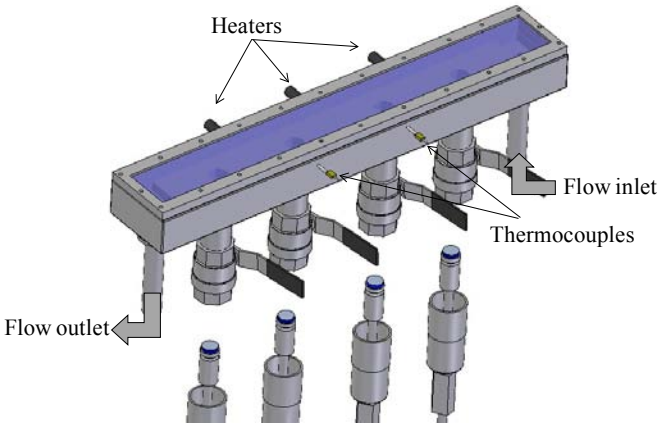

Figure 1: Schematic Representation of the Test Section of the TCFC, which is part of a circulating flow loop

Table 1
Experimental Conditions, Parameters for Electrochemical Measurements and Techniques used for Surface Analysis.

Operating parameters	**Conditions**
Test solution	3 wt.% NaCl
Test material	API 5L X65, UNS G10180
Temperature	80°C
Total pressure	1 bar
pCO_2	0.54 bar
pH	6.0 ± 0.10
Velocity	0.5 m s^{-1}
Electrochemical measurements	LPR
Scan range	±5 mV
Scan rate	0.125 mV s^{-1}
Surface analysis	SEM, EDS

Electrochemical Probes and Sample Preparation

Prior to immersion into the TCFC, the mild steel electrochemical probe (Figure 2a) used for electrochemical measurements and three samples (Figure 2b) used for surface and chemical analysis, were ground by silicon carbide paper to a 600 grit surface finish and rinsed with isopropyl alcohol. The concentric ring style electrochemical probe has a working electrode (WE) with a 0.95 cm^2 exposed area. For surface layer observations, API 5L X65 and UNS G10180 mild steels were machined into a cylindrical shape of 3.17 cm diameter and 0.64 cm length, with the sides and back of the sample coated with Teflon, leaving a single 7.9 cm^2 exposed surface area. For cross section analysis, the steel samples were mounted in epoxy resin, cut with a diamond saw, polished with diamond suspension and sputtered with gold. Chemical compositions of the API 5L X65 and UNS G10180 steels are shown in Table 2. Figure 3 shows the microstructure of the carbon steel used in the tests. The API 5L X65 samples (Figure 3a) consisted of a tempered martensite microstructure with carbides in the shape of small spheroidized particles in the grain boundaries. On the other hand, UNS G10180 samples (Figure 3b) have a ferrite - pearlite microstructure.

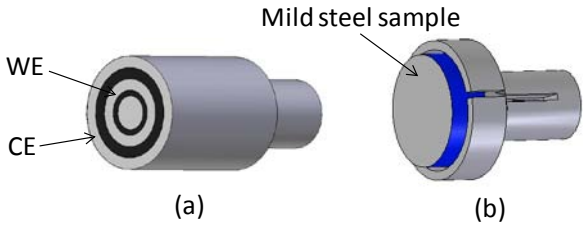

Figure 2: (a) LPR Probe Head and (b) cylindrical mild steel sample. For placement in test section, see Figure 1

Table 2
Chemical Composition of API 5L X65 and UNS G10180 Steels (wt.%)

API 5L X65 mild steel (balance Fe)

Al	As	C	Co	Cr	Cu	Mn	Mo	Nb	Ni	P
0.033	0.015	0.140	0.012	0.150	0.140	1.180	0.160	0.027	0.380	0.012
S	**Sb**	**Si**	**Sn**	**Ti**	**V**	**Zr**				
0.003	0.035	0.250	0.012	0.002	0.052	0.004				

UNS G10180 mild steel (balance Fe)

Al	As	C	Co	Cr	Cu	Mn	Mo	Nb	Ni	P
0.001	0.007	0.160	0.010	0.063	0.250	0.790	0.020	0.006	0.078	0.008
S	**Sb**	**Si**	**Sn**	**Ti**	**V**	**Zr**				
0.029	0.011	0.250	0.017	<0.001	0.001	0.004				

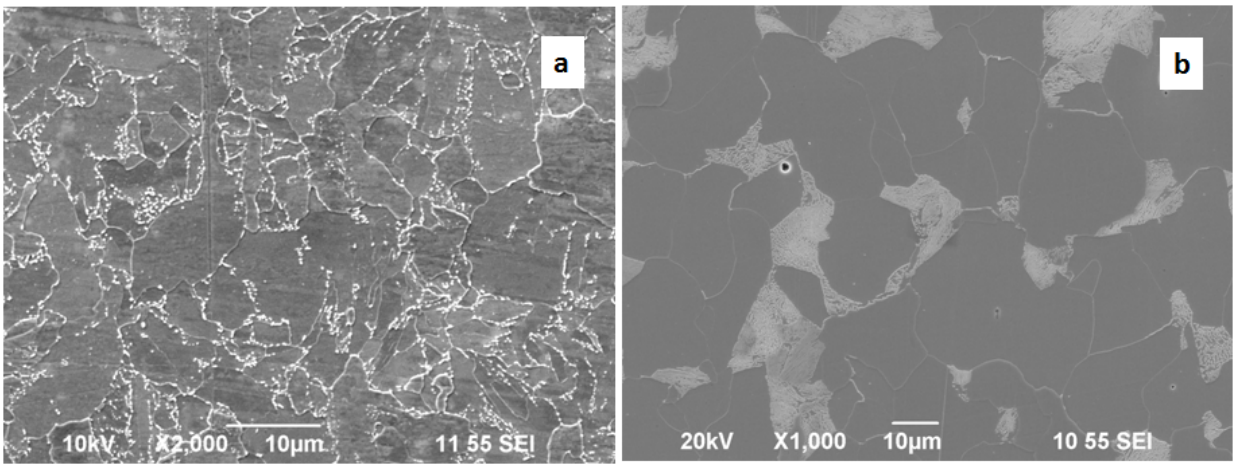

Figure 3: SEM Images of the Microstructure of the Carbon Steels Used in the Tests (2% Nital Etched): (a) API 5L X65 - Tempered Martensite, (b) UNS G10180 Ferrite – Pearlite

Electrochemical Measurements

LPR measurements were performed using a Gamry† PCI4/300 Potentiostat/Galvanostat/ZRA. For the LPR measurements, the working electrode was polarized ±5 mV versus the open circuit potential using a scan rate of 0.125 mV s^{-1}. The polarization resistance, Rp, was used to calculate the current density (j_{corr}) by using the Stern-Geary equation.[12] The resulting j_{corr} was converted into corrosion rate using Equation (1):[13]

$$\text{Corrosion rate(mm/year)} = \frac{0.00327 \times j_{corr}(\mu\text{A/cm}^2) \times \text{EW}}{\text{density(g/cm}^3)} \quad (1)$$

where 0.00327 is a constant factor used unit conversion and EW is the equivalent weight of iron in grams. The B" of 26 mV was used in this work.

Surface Characterization

SEM analyses were performed on a JEOL† JSM-6390LV instrument. Chemical composition of the corrosion product was recorded by an EDS detector that is coupled to the SEM.

RESULTS AND DISCUSSION

Tempered Martensite Microstructure – X65 Steel

The corrosion rate and corrosion potential for an X65 steel observed during 258 h of exposure to a 3 wt.% solution saturated with CO_2, 80ºC and 0.5 m s^{-1} is shown in Figure 4. The saturation value of $FeCO_3$ calculated based on iron concentration measurements and a water chemistry model is shown as well. S_{FeCO3} represents the saturation value in the bulk. Three different stages are clearly identified: Active corrosion, Nucleation and Growth of $FeCO_3$ and Pseudo – passivation stage.

† Trade name.

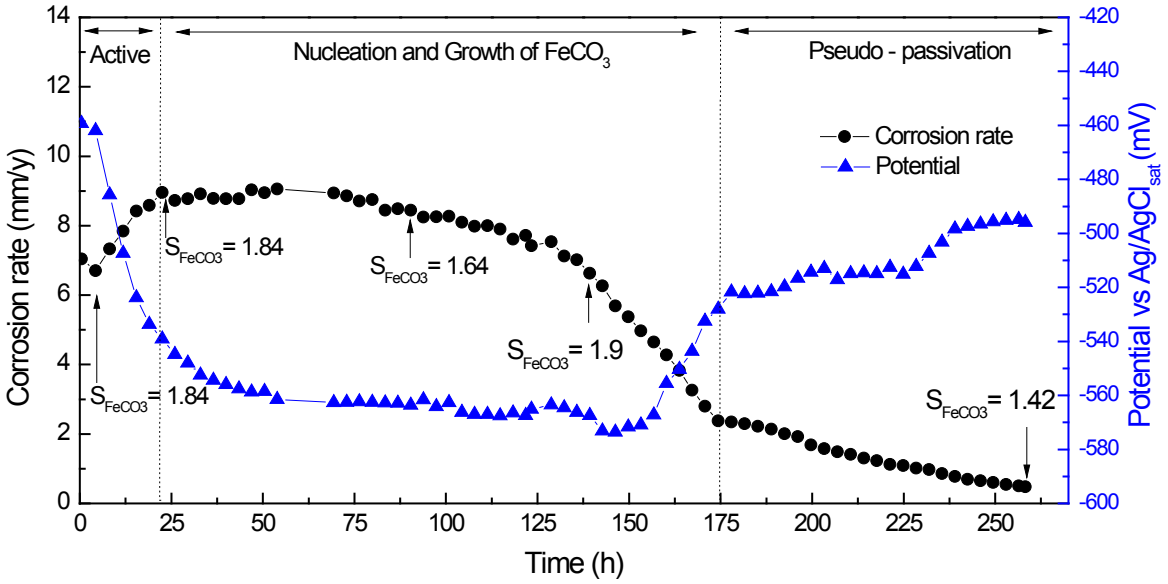

Figure 4: Change in Corrosion Rate and Corrosion Potential with Time during the Formation of a Porous Fe_3C Layer and Protective $FeCO_3$ on API 5L X65 Mild Steel with a Tempered Martensite Microstructure (3wt.% NaCl Aqueous Solution, 80ºC, pH 6, 0.5 m s^{-1})

Active Corrosion Stage

The active stage is characterized by a sharp increase in the corrosion during the first 22 h of exposure. The initial corrosion was 7 mm y^{-1} and increase to 8.9 mm y^{-1} during this period. The steep increase in corrosion rate can be attributed to presence of ferrite and Fe_3C in the steel. It has been reported that Fe_3C can accelerate the corrosion rate since it is possible for Fe_3C to assume the role of a cathodic site while ferrite corrodes.[14] According to the metallographic analysis of the X65 steel (Figure 3a), carbides are present in a globular shape on the grain boundaries. As the corrosion process keeps going, more carbides are exposed, increasing the cathodic surface and therefore the corrosion rate.

Nucleation and Growth of $FeCO_3$ Stage

The corrosion rate from 22 to 69 h remained relatively constant at 8.9 mm y^{-1}. During this period, one of the API 5L X65 samples was taken out of the thin channel flow cell for surface observation and chemical analysis. Figure 5a shows a top view and chemical analysis of the corrosion product found after 41 h. The appearance of the corrosion layer was gray to black, typical of Fe_3C layers.[15] It is possible that the cracks were caused during the drying process of the sample. Considering that this surface has been formed after the preferential dissolution of the ferrite phase over cementite, the presence of alloying elements should be expected on the porous layer. The EDS analysis showed the presence of Ni, Mo, V, Cr, Cu and Mn, elements that are part of the chemical composition of the X65 steel (Table 2). Several authors have found cementite layers rich in alloying elements.[7, 16, 17]

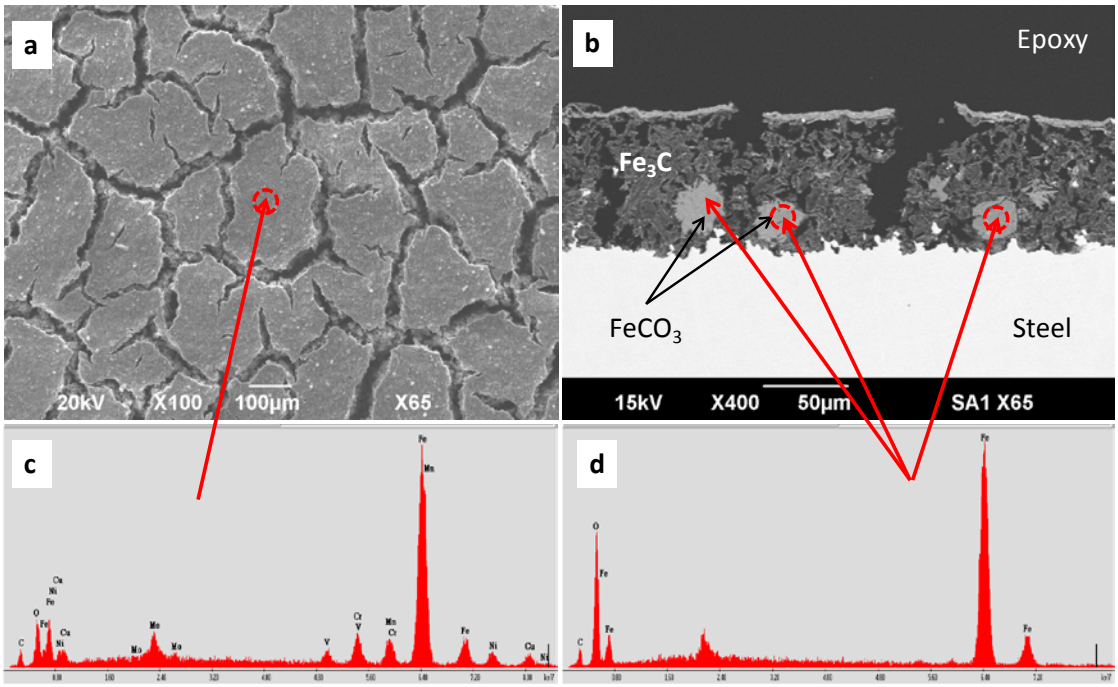

Figure 5: API 5L X65 Sample after 41 h of Exposure in a 3wt.% NaCl Aqueous Solution, 80°C, 0.5 m s^{-1}, pH 6. SEM Images of (a) Top View and (b) Cross Section with the Respective EDS Analysis (c) and (d)

A cross section view of the sample, Figure 5b, revealed the presence of a ~80 µm thick porous layer. It is important to point out that the average LPR corrosion rate at 41 h was ~ 8 mm y^{-1}, corresponding to 37.4 µm of metal loss, which is about half the of the thickness of the corrosion product shown in Figure 5b. This suggests that LPR is not able to correctly measure the corrosion rate in the presence of Fe_3C layer due to the galvanic effect. It can be appreciated as well the scatter presence of a second phase inside the carbide layer which EDS analysis shows the presence of carbon, oxygen and iron, suggesting the presence of $FeCO_3$. The unlabeled pick corresponds to the gold used for sputtering the samples. The presence of some $FeCO_3$ during this period corroborates that the water chemistry inside the porous later is different from the bulk.

After 69 h, a change in the trend of the corrosion rate was observed (Figure 4). The corrosion rate slowly started to decrease from 8.9 mm y^{-1} to 7.5 mm y^{-1} at 128 h of exposure. Afterwards, a sharp decrease in the corrosion rate happened, reaching 2.3 mm y^{-1} after 174 h.

The behavior observed from 22 h to 174 h in Figure 4 can be attributed to the nucleation and growth of a protective scale with time. In order to corroborate that hypothesis, another sample was taken out of the system at 175 h. Figure 6a shows a top view of the corrosion product found in the API 5L X65 sample that looks similar to the SEM image shown in Figure 5a. No $FeCO_3$ crystals were observed on top of the surface that could explain the decrease in corrosion rate. Further SEM and EDS analysis helped in answering that question. Figure 6b shows a cross section view of the same sample taken after 175 h, and Figure 6c a magnification of the marked area in Figure 6b. Backscattered electrons were used for taking the SEM images in order to distinguish between areas with different chemical composition. It can be seen a second phase distributed evenly along the entire metal surface between the metal and porous layer with a thickness of ~50µ. The EDS analysis suggests that this layer was mainly composed of iron carbonate. Farelas[18] reported XRD analysis showing the presence of cementite and iron carbonate in X65 samples exposed to similar experimental conditions.

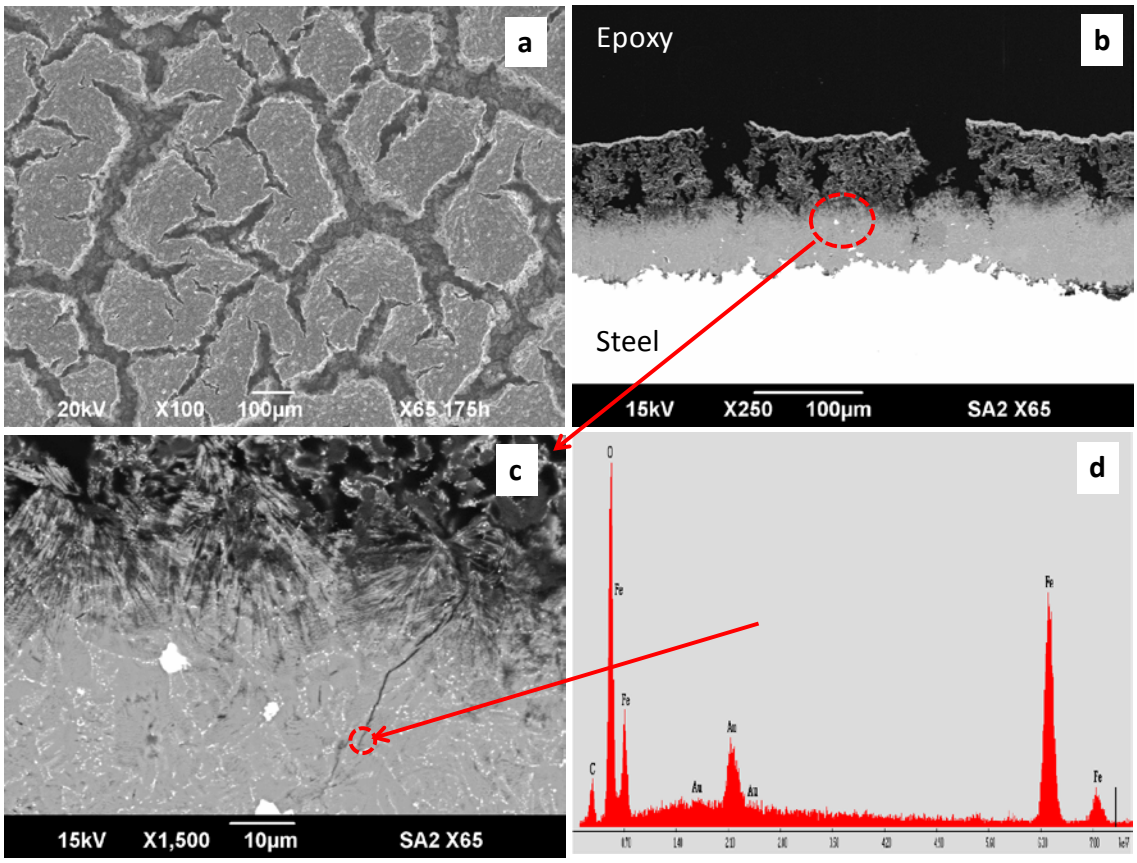

Figure 6: API 5L X65 steel after 175 h of exposure in a 3wt.% NaCl aqueous solution, 80ºC, 0.5 m s^{-1}, pH 6. SEM images of (a) top view, (b) cross section, (c) the magnified detail of the cross section and (d) EDS analysis of the corrosion product layer

When the concentration of [Fe^{2+}] and [CO_3^{2-}] exceeds its solubility limit, $FeCO_3$ can form according to Equation 2.

$$Fe^{2+} + CO_3^{2-} \rightarrow FeCO_3 \quad (2)$$

An important parameter for the precipitation of $FeCO_3$ is the saturation value of iron carbonate (S_{FeCO_3}) that can be calculated by Equation 3.

$$S_{FeCO_3} = \frac{[Fe^{2+}][CO_3^{2-}]}{K_{sp}} \quad (3)$$

where [Fe^{2+}] is the measured concentration of ferrous ions in solution; [CO_3^{2-}] is the equilibrium concentration of the carbonate ions calculated using an equilibrium water chemistry model;[19] K_{sp} is the solubility product for $FeCO_3$ which is a function of temperature and ionic strength.[20]

It has been published that high supersaturation values are needed in order to initiate the formation of $FeCO_3$.[21] Figure 4 shows the saturation value of $FeCO_3$ in the 3% NaCl solution at different times during the test calculated with Equation 3. The saturation values are low and almost constant during the entire tests, explaining why no $FeCO_3$ crystals were observed on top of the corrosion product. On the other hand, inside the porous layer shown in Figure 6b and Figure 6c, nearly stagnant conditions are achieved and the composition of the solution in contact with the metal changes. High pH and high $FeCO_3$ saturation can be found close to the metal surface, since the porous layer restricts the transport of reactants in and corrosion products out. Such local conditions favor the formation of a protective $FeCO_3$ layer, resulting in a decrease in the corrosion rate and an increase in the corrosion potential

(Figure 4). It is important to point out that the protective scale preserved the original tempered martensite microstructure with the small spheroidized carbide particles (Figure 6c).

Pseudo-passivation Stage

After 175 h, the corrosion rate kept decreasing, as it can be observed by a change in the slope in the corrosion rate in Figure 4. The formation rate of $FeCO_3$ slowed down because most the Fe^{2+} ions were consumed during the growth of $FeCO_3$. However, more ferrous ions are still being released due to the corrosion process and consumed during the formation of more $FeCO_3$ and growth of the existing scale. As a consequence, the corrosion rate decreased from 2.3 mm y^{-1} to 0.4 mm y^{-1} at the end of the test (258 h). During this period, the corrosion potential kept increasing (Figure 4), an effect that can be attributed to the decrease of the anodic reaction due to the blockage effect of $FeCO_3$ on the steel surface. Figure 7 shows the SEM pictures and EDS analysis of the corrosion product found after 258 h. Similar to the sample observed after 175 h, no $FeCO_3$ crystals were observed on top of the surface (Figure 7a). Cross section SEM images, Figure 7b and Figure 7c, showed the presence of $FeCO_3$ layer between the steel surface and the porous layer with a thickness of ~75 µm.

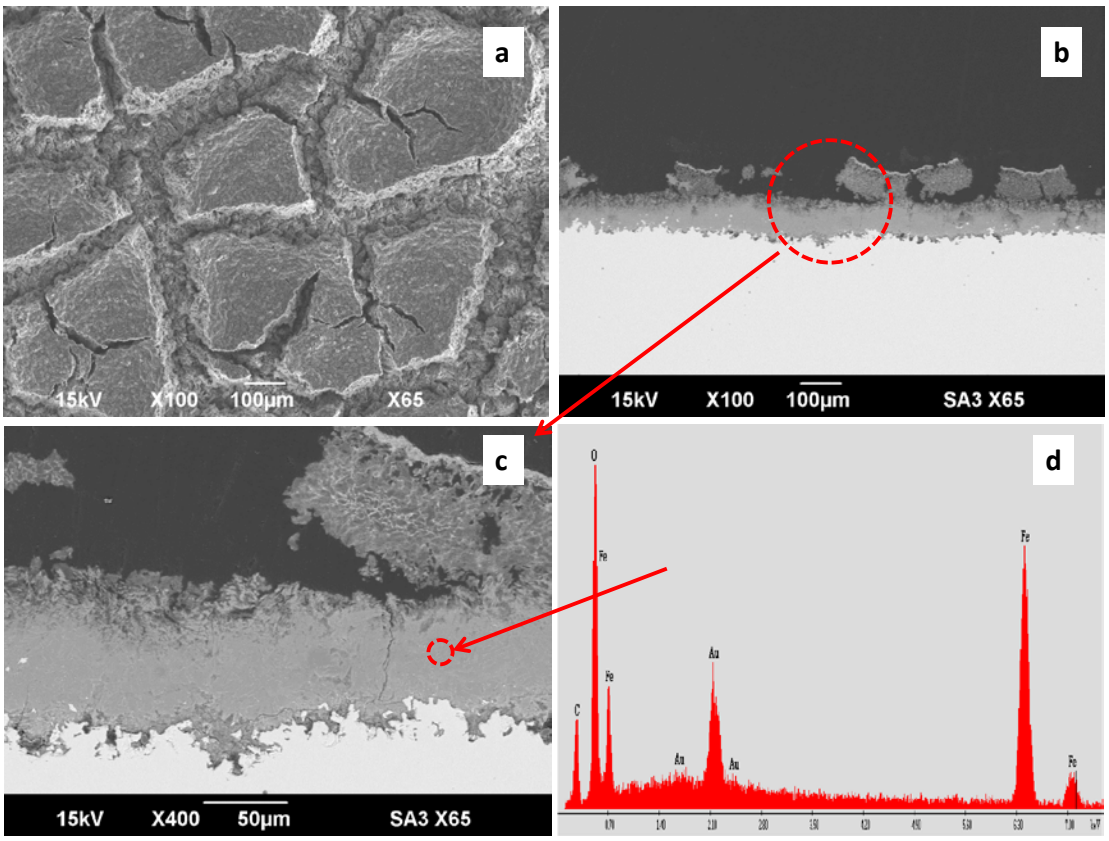

Figure 7: API 5L X65 steel after 258 h of exposure in a 3wt.% NaCl aqueous solution, 80ºC, 0.5 m s^{-1}, pH 6. SEM images of (a) top view, (b) cross section, (c) the magnified detail of the cross section and (g) EDS analysis of the corrosion products layer

Ferrite - Pearlite Microstructure – UNS G10180 Steel

Figure 8 shows the corrosion rate and potential change with time for a UNS G10180 steel with a ferrite - pearlite microstructure. The same corrosion trend was observed as in steels with tempered martensite microstructure (Figure 4). Three different stages are clearly identified: Active, nucleation and growth of $FeCO_3$ and pseudo–passivation stage.

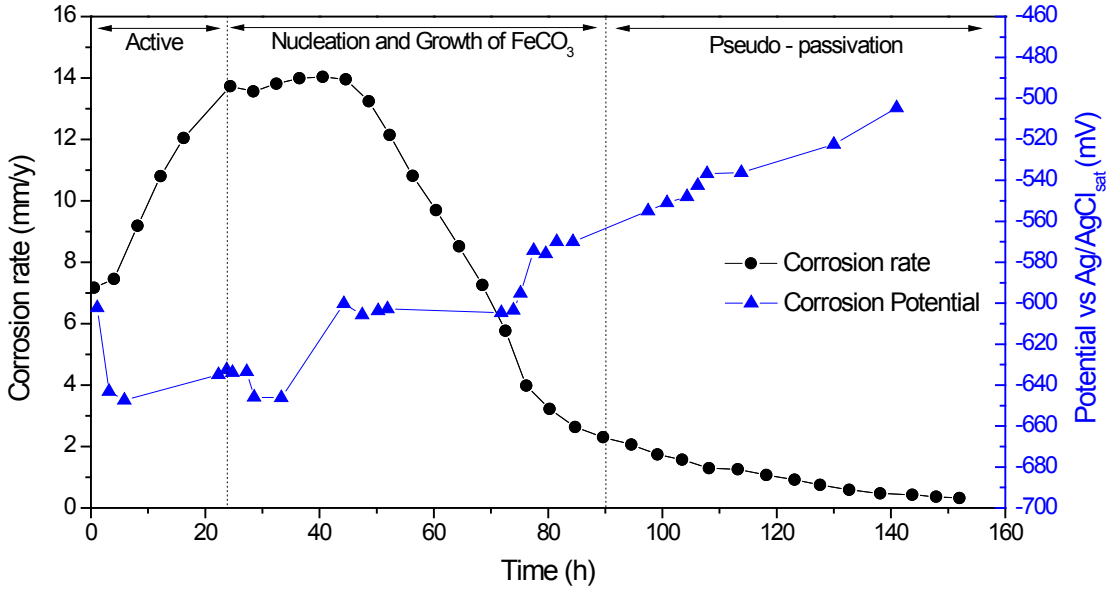

Figure 8: Change in Corrosion Rate and Corrosion Potential with Time during the Formation of a Porous Fe_3C and Protective $FeCO_3$ on a UNS G10180 Carbon Steel with Ferrite - Pearlite Microstructure (3wt.% NaCl Solution, 80ºC, pH 6, 0.5 m s^{-1})

Active Corrosion Stage

For the case of the UNS G10180 steel the initial corrosion rate was 7.1 mm y^{-1} and increased to 13.7 mm y^{-1} during the first 24 h of exposure, 4.8 mm y^{-1} higher than the corrosion rate observed on the API 5L X65 steel during the same stage. The UNS G10180 steel microstructure (Figure 3b) shows that the lamellar pearlite is well – distributed increasing the contact area between the pearlite and the ferrite grains. It has been stated that the Fe_3C present in the pearlite phase is more noble than the ferrite phase, leading to microgalvanic cells.[11] As a consequence, ferrite corrodes over Fe_3C, leaving a higher cathodic area (Fe_3C) with time, explaining the increase in the corrosion rate.

Nucleation and Growth of $FeCO_3$ Stage

After 24 h, the corrosion rate remained constant at around 13.8 mm y^{-1} for 20 h. Figure 9a shows a top view of the corrosion product found in one of the UNS G10180 samples taken out of the system after 41 h when the corrosion rate was high. A porous layer enriched with alloying elements can be appreciated. The UNS G10180 microstructure shown in Figure 3b showed that the pearlite phase forms a well defined network. Therefore, the formation of a porous carbide layer should be expected as a consequence of the preferential dissolution of ferrite. A cross section view (Figure 9b) showed a porous layer of approximately 73 µm thick. As in the previous case, the metal loss calculated base on the average LPR corrosion rate at 41 h (11.6 mm y^{-1}) did not corresponded to the thickness of the Fe_3C layer observed in Figure 9b. This corrosion rate should have produced a 53.8 µm Fe_3C layer which is smaller than the shown in Figure 9b. This observation suggests again that LPR is not able to correctly measure the corrosion rate in the presence of Fe_3C and that microstructure also has influence on the LPR readings. The latter can be corroborated by comparing the thickness of the Fe_3C layer shown in Figure 5b and Figure 9b which are similar, therefore similar corrosion rates should expected on both steels at 41 h of exposure.

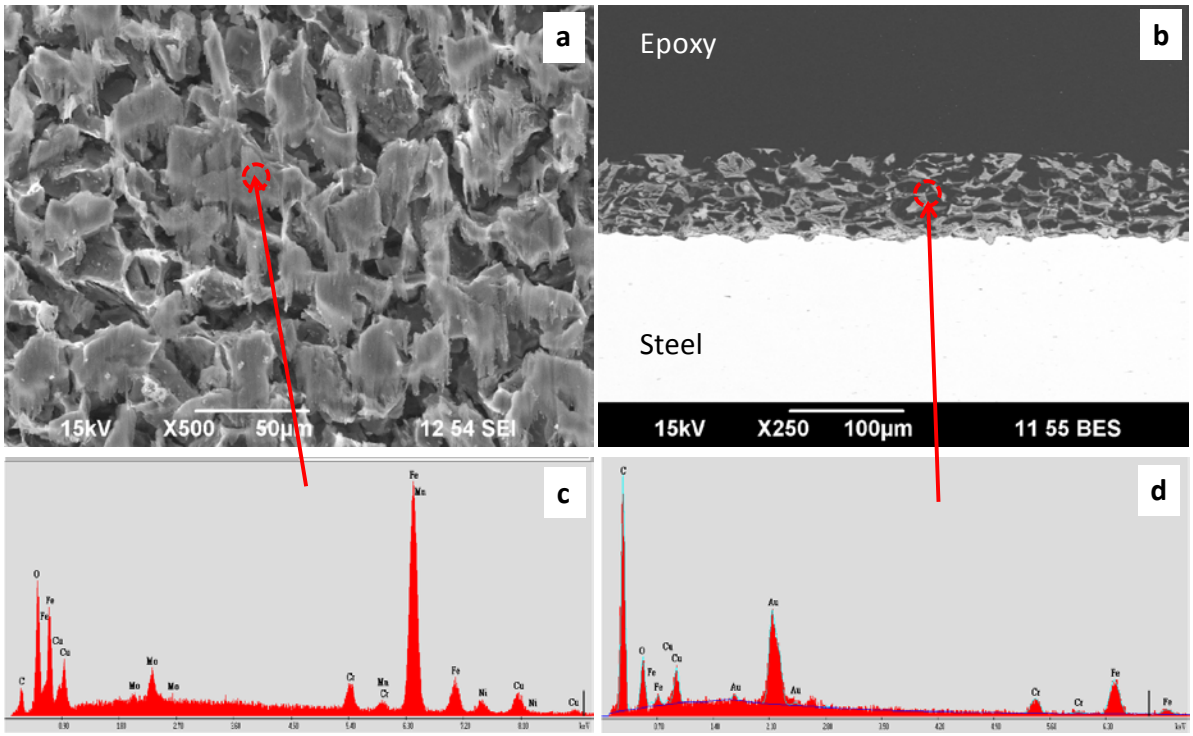

Figure 9: UNS G10180 steel after 41 h of exposure in a 3wt.% NaCl aqueous solution, 80ºC, 0.5 m s^{-1}, pH 6. SEM images of the (a) top view and (b) cross section view, with the respective EDS analysis (c) and (d)

The high corrosion rate observed in the ferrite – pearlite steel allowed the formation of a thick Fe_3C layer. As a result, optimal conditions for the formation of $FeCO_3$ (high pH and $FeCO_3$ saturation values) were achieved inside the porous layer and after 45 h of exposure the corrosion rate decreased sharply from 13.9 mm/y to 2.3 mm y^{-1}. It important to mention that this process occurred faster in the UNS G10180 steel than the API 5L X65. Figure 10a shows a top view of the corrosion product found after 90 h of exposure. No $FeCO_3$ crystals were observed that could explain the decrease in corrosion rate. A cross section picture (Figure 10b) revealed the presence of a second phase inside the porous Fe_3C layer. The EDS analysis shows the presence of carbon, oxygen and iron, suggesting the presence of $FeCO_3$. The inner layer preserved the pearlite morphology of the original steel and it is more evident in Figure 10c.

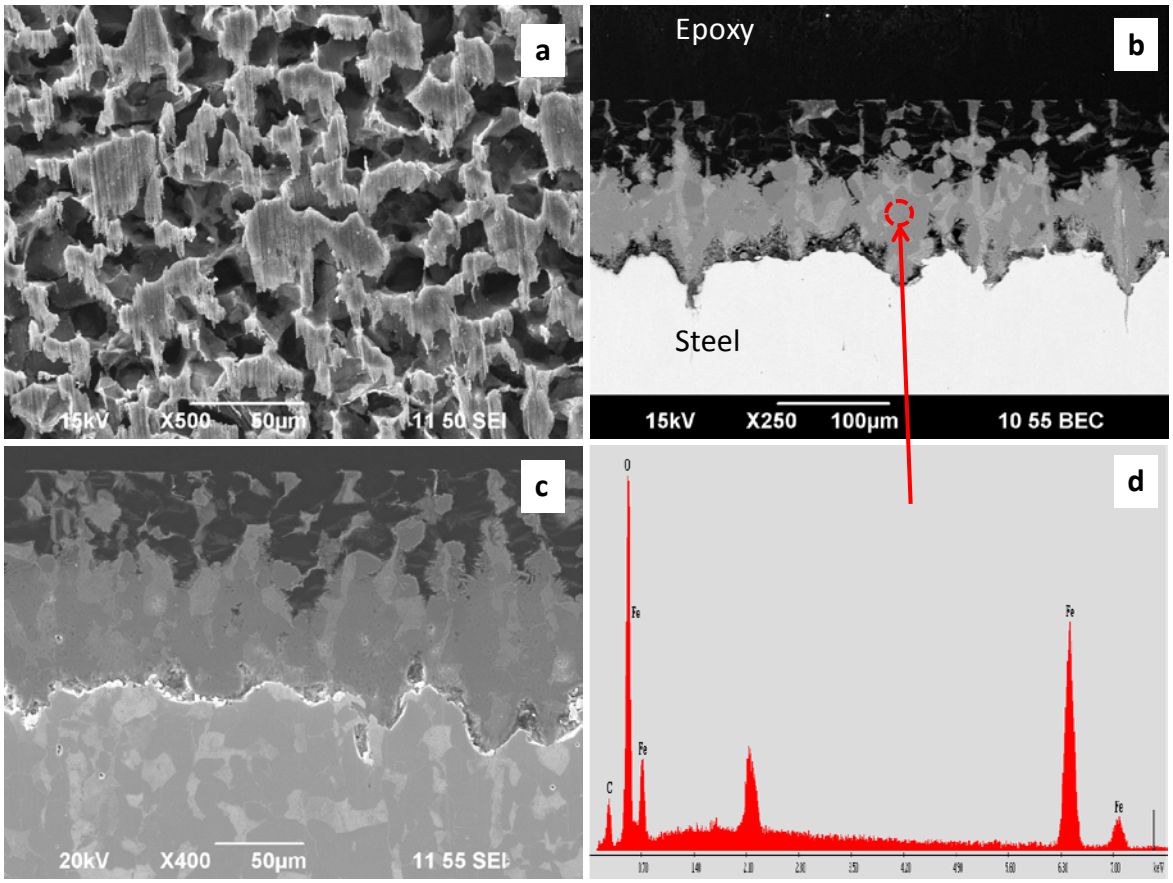

Figure 10: UNS G10180 steel after 90 h of exposure in a 3wt.% NaCl aqueous solution, 80ºC, 0.5 m s^{-1}, pH 6. SEM images of the (a) top view and (b), (c) cross section, and (d) corresponding EDS analysis of the corrosion product layer. The steel surface cross section (c) was etched with 2% Nital

Pseudo – passivation Stage

After 90 h, most of the protective $FeCO_3$ had already formed, decreasing in a big extent the cathodic areas (Fe_3C) and also blocking the active metal surface as it was shown by an increase in the corrosion potential. The corrosion rate kept slowly decreasing because the $FeCO_3$ continued growing and filling empty spaces during this stage. Figure 11 shows a top view and cross section images of a sample taken out of the TCFC after 150 h. No $FeCO_3$ crystals were observed on top of the surface (Figure 11a). The cross section analysis (Figure 11b) revealed a denser $FeCO_3$ scale inside the porous cementite that is covering almost the entire metal surface. At the end of the test (152 h), the corrosion rate was measured to be 0.3 mm y^{-1}.

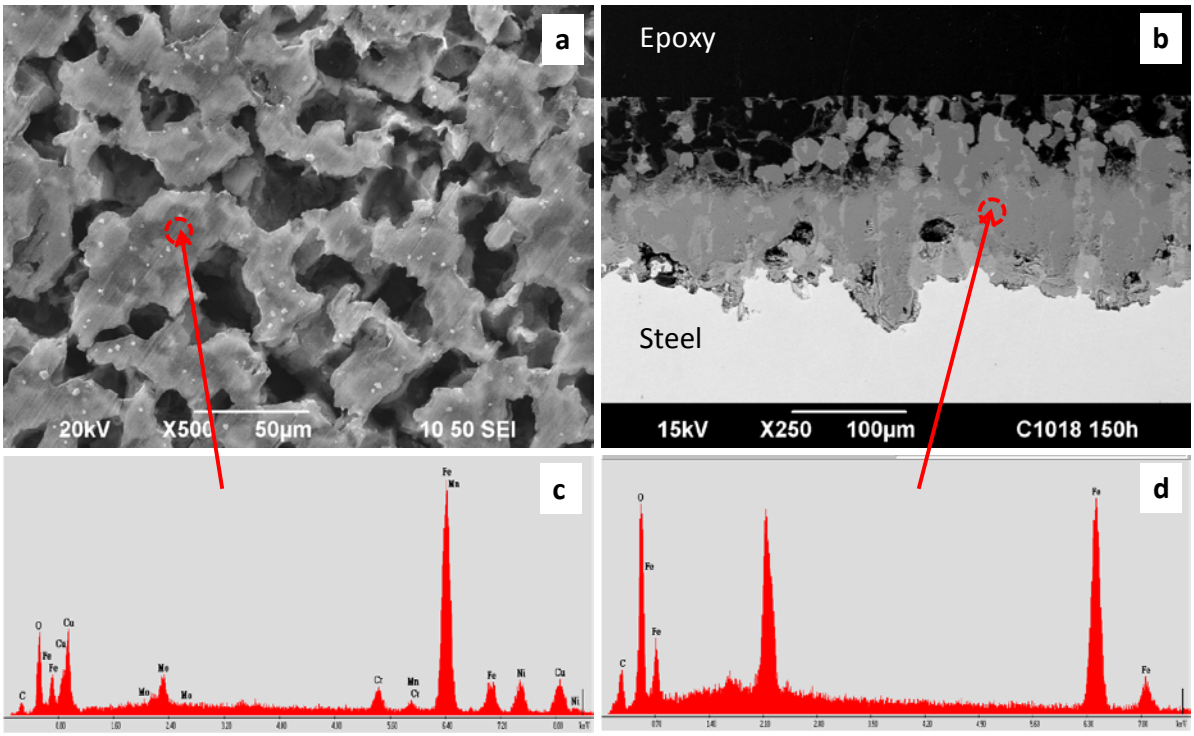

Figure 11: UNS G10180 steel after 150 h of exposure in a 3wt.% NaCl aqueous solution, 80ºC, 0.5 m s^{-1}, pH 6. SEM images of the (a) top view and (b) cross section with the respective EDS analysis (c) and (d)

CONCLUSIONS

In this study, long term experiments were performed using two mild steels with tempered martensite and ferrite - pearlite microstructures, respectively. Mild steel samples were exposed to a 3% NaCl CO_2 saturated solution at pH 6, 80°C and under flowing condition. Based on the results obtained, the following conclusions can be drawn:

- Regardless of the steel microstructure, three different stages were indentified under the experimental conditions of this study: active corrosion, nucleation and growth of $FeCO_3$ and pseudo-passivation stages.
- During the active stage, both mild steels formed a porous Fe_3C layer which is responsible for the increase in corrosion rate due to a galvanic effect.
- During the following stage the corrosion rate decreased as the $FeCO_3$ formed within the pores of the Fe_3C layer, regardless of the bulk $FeCO_3$ saturation value.
- Formation of protective $FeCO_3$ continued in the last stage accompanied by an increase in corrosion potential.
- The formation of the Fe_3C layer created favorable conditions at the steel surface for protective $FeCO_3$ to form, which was otherwise not favoured based on the bulk water chemistry.

REFERENCES

1. D. A. López, S. N. Simison, S.R. de Sánchez, The influence of steel microstructure on CO_2 corrosion. EIS studies on the inhibition efficiency of benzimidazole, Electrochimica Acta 48 (2003) p. 845-854.
2. D. A. López, T. Pérez, S. N. Simison, The influence of microstructure and chemical composition of carbon and low alloy steels in CO_2 corrosion. A state-of-the-art appraisal, Materials and Design 24 (2003) p. 561-575.
3. M. B. Kermani, A. Morshed, Carbon Dioxide Corrosion in Oil and Gas Production – A Compendium, Corrosion 59, 8 (2003) p. 659.
4. S. H. Avner, Introduction to Physical Metallurgy, Second Edition, 1998, McGraw.Hill.
5. J. Crolet, N. Thevenot, S. Nesic, Role of Conductive Corrosion Products in the Protectiveness of Corrosion Layers, Corrosion 54 (1998) p. 194.
6. K. Videm, J. Kvarekvaal, T. Perez, G. Fitzsimons, Surface effects on the Electrochistry of Iron and Mild steel Electrodes in Aqueous CO2 Solutions, CORROSION/96, Paper No. 1, NACE, Houston, TX, 1996.
7. A. Dugstad, Mechanism of Protective Layer Formation During CO_2 Corrosion of Mild steel, CORROSION/98, Paper No. 31, NACE, Houston, TX, 1998.
8. C. A. Palacios and J. R. Shadley, Characteristics of Corrosion Scales on Steels in a CO_2-Saturated NaCl Brine, Corrosion 74 (2) (1991) p. 122.
9. T. Berntsen, T. Hemmingsen, M. Seiersten, Effect of $FeCO_3$ Supersaturation and Carbide Exposure on the CO_2 Corrosion Rate of Carbon Steel, CORROSION/2011, Paper No. 11072, NACE, Houston, TX, 2011.
10. W. Farida, T. Hemmingsen, T. Berntsen, P. Rabindran, Effect of Precorrosion and Temperature on the Formation Rate of Iron Carbonate Film, 7th Pipeline Technology Conference 2012, p. 1-16.
11. S. Al-Hassan, B. Mishra, D. L. Olson, and M. M. Salama, Effect of Microstructure on Corrosion of Steels in Aqueous Solution Containing Carbon Dioxide, Corrosion 54 (6) (1998) p. 480.
12. M. Stern and A. L. Geary, Electrochemical polarization I. A theoretical analysis of the shape of polarization curves, J. Electrochem. Soc. 104 (1957) p. 56.
13. J. R. Scully and R. G. Kelly, Methods for determining aqueous corrosion reaction rates, Corrosion: Fundamentals, testing and protection, Vol 13A, ASM Handbook, ASM International, 2003, p. 68-86.
14. N. Staicopolus, The Role of Cementite in the Acidic Corrosion of Steel, J. Electrochem. Soc., 110, (1963).
15. K. Videm, “The Influence of pH and Concentration of Bicarbonate and Ferrous ions on the CO_2 Corrosion of Mild steels,” CORROSION/93, Paper No. 83, (Houston, TX: NACE, 1993).
16. K. Videm, J. Kvarekvaal, T. Pérez and G. Fitzsimons, “Surface Effects on the Electrochemistry of Iron and Mild steels Electrodes in Aqueous CO_2 Solutions”, CORROSION/96, Paper No. 1, (Houston, TX: NACE, 1996).
17. E. Gulbrandsen, S. Nesic, A. Stangeland, T. Burchardt, “Effect of Precorrosion on the Performance of Inhibitors for CO_2 Corrosion of Mild steel”, CORROSION/98, Paper No. 13, (Houston, TX: NACE, 1998).

18. F. Farelas, Electrochemical Study of the Evolution of Dissolution and Inhibition Processes at the Interface of 1018 and X65 Carbon Steel Exposed to CO_2 Environments using a Linear Flow Cell and a Rotating Cylinder Electrode, Ph.D. dissertation, Instituto Mexicano del Petroleo (2010).

19. M. Nordsveen, S. Nesic, R. Nyborg, and A. Stangeland, A mechanistic model for carbon dioxide corrosion of mild steel in the presense of protective iron carbonate films – Part 1: theory and verification, Corrosion 59, 5 (2003) p. 443.

20. W. Sun, S. Nesic and R. C. Woollam, The Effect of Temperature and Ionic Strength on Iron Carbonate ($FeCO_3$) Solubility Limit, Corr. Sci. 51 (2009) p. 1273-1276.

21. K. Chokshi, W. Sun, S. Nesic, Iron Carbonate Scale Growth and the Effect of Inhibition in CO_2 corrosion of Mild Steel, CORROSION/2005, Paper No. 5285, (Houston, TX: NACE, 2005).